Cell Reports
Physical Science

CellPress
OPEN ACCESS

Article

Ultrafast synthesis of high-entropy carbides up to 3,273 K for superior oxidation resistance

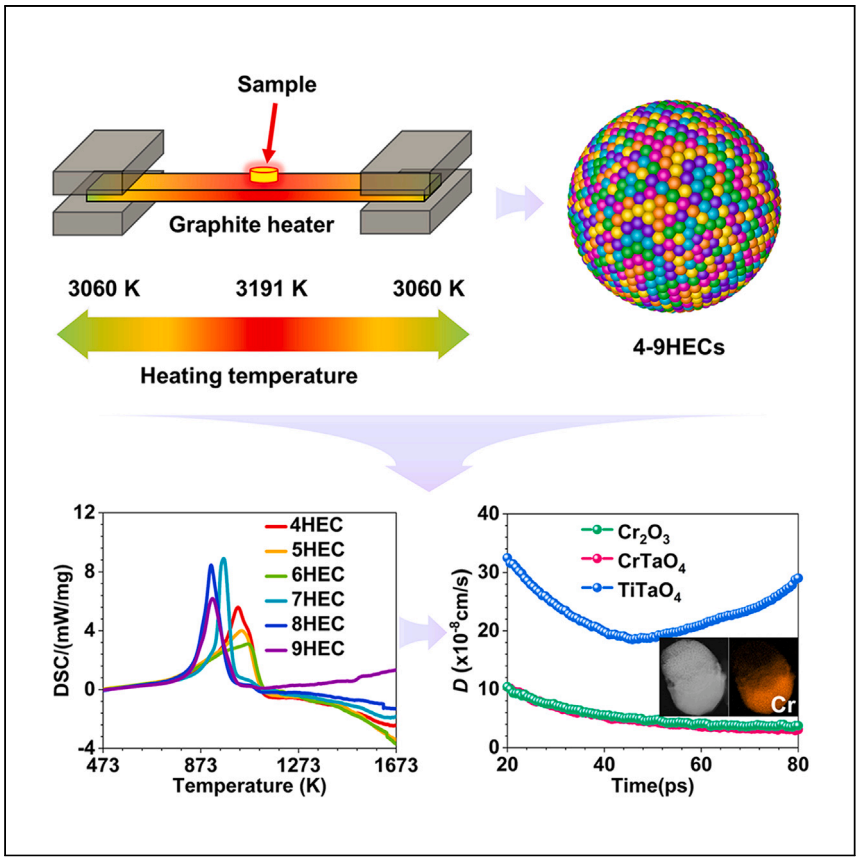

Wen et al. successfully fabricate 4- to 9-cation high-entropy carbides (HECs) via an ultrafast high-temperature synthesis apparatus and perform composition screening for superior oxidation resistance through thermal gravimetric analysis and first-principles calculations. This research demonstrates the composition screening and optimization process for HECs.

Zihao Wen, Zhongyu Tang, Hong Meng, Lei Zhuang, Hulei Yu, Yanhui Chu

lzhuang@scut.edu.cn (L.Z.)
chuyh@scut.edu.cn (Y.C.)

Highlights

Ultrafast high-temperature synthesis (UHTS) apparatus up to 3,273 K is developed

4- to 9-cation high-entropy carbides are successfully fabricated by UHTS

6-cation high-entropy carbides show the best oxidation resistance

Superior oxidation resistance is owed to (Cr, Me)(Ta, Me)O_4 and (Cr, Me)$_2O_3$ layers

Wen et al., Cell Reports Physical Science 5, 101821
February 21, 2024
https://doi.org/10.1016/j.xcrp.2024.101821

Cell Reports
Physical Science

CellPress
OPEN ACCESS

Article

Ultrafast synthesis of high-entropy carbides up to 3,273 K for superior oxidation resistance

Zihao Wen,[1,2] Zhongyu Tang,[1,2] Hong Meng,[1] Lei Zhuang,[1,*] Hulei Yu,[1] and Yanhui Chu[1,3,*]

SUMMARY

Exploiting the huge compositional space is significant in achieving the superior oxidation resistance of high-entropy carbides (HECs) yet is challenging with conventional synthesis techniques. Herein, we develop an ultrafast high-temperature synthesis apparatus to reach a heating temperature of 3,273 K within seconds. Based on this apparatus, the equiatomic 4- to 9-cation HECs of the IVB, VB, and VIB groups with compositional uniformity are synthesized via carbothermal reduction. The oxidation resistance of all the as-synthesized HEC samples is then investigated via thermogravimetric analysis. The results show that the 6-cation HEC samples possess the best oxidation resistance. Their superior oxidation resistance is attributed to the formation of (Cr, Me)(Ta, Me)O_4 and (Cr, Me)$_2O_3$ (Me = Hf, Zr, Ta, Nb, Ti, and Cr) protective layers, which are experimentally and theoretically proved to effectively inhibit the inward diffusion of oxygen. Such superior oxidation resistance enables potential applications in extreme environments.

INTRODUCTION

Since their discovery in 2015, high-entropy ceramics have gained increasing attention in the ceramic community because of their immense compositional space, unique microstructural features, and tunable properties.[1–3] So far, a great deal of effort has been devoted to developing many kinds of high-entropy ceramics, including high-entropy oxides,[1,3–5] high-entropy borides,[6–10] and high-entropy carbides (HECs).[11–19] Particularly, owing to the unique chemical and physical properties of individual components, such as ultrahigh melting point over 3,273 K, high hardness, and good oxidation resistance, HECs are considered the most attractive for high-temperature structural applications, e.g., rocket nozzles and hypersonic vehicles, where thermal stability, mechanical properties, and oxidation resistance are in great demand.[13,17] To date, the mechanical and thermal properties of HECs have been extensively studied and proved to outperform their individual components.[2,11,17,20] Despite these properties, the potential high-temperature applications of HECs also place a high priority on the oxidation resistance at elevated temperatures. However, there is limited literature devoted to the oxidation resistance of HECs.[21–27] In general, the oxidation resistance of HECs is inferred to be tunable, mainly depending on their compositions. The current oxidation resistance of the developed HECs still cannot meet the demand for high-temperature structural applications. Therefore, exploiting the superior oxidation resistance of HECs is significant for achieving their potential high-temperature structural applications. The vast compositional space of HECs endows them with great potential of having superior oxidation resistance, yet the wide range of possible compositions and the complexity of the atomic arrangements still pose grand challenges in fabricating HECs with rich elemental compositions.

[1]School of Materials Science and Engineering, South China University of Technology, Guangzhou 510641, China

[2]These authors contributed equally

[3]Lead contact

*Correspondence: lzhuang@scut.edu.cn (L.Z.), chuyh@scut.edu.cn (Y.C.)

https://doi.org/10.1016/j.xcrp.2024.101821

Up to now, a number of synthesis techniques have been developed to fabricate HECs, including carbothermic reduction,[28,29] molten salt synthesis,[30] and combustion synthesis.[16] However, most of the research has focused on HECs with no more than six metal elements, which severely constrained the compositional space of HECs. It is well known that incorporating more atoms with significantly different atomic radii contributes to greater distortions in a single sublattice, leading to element or phase segregation.[31,32] Therefore, a higher synthesis temperature is required to increase the elemental diffusion coefficients and acquire a uniform elemental distribution of HECs. Unfortunately, the typical temperature of conventional ceramic synthesis techniques does not exceed 2,573 K, which restricts the compositional enrichment of HECs. Recently, an ultrafast high-temperature synthesis (UHTS) technique based on strong Joule heating has been developed to synthesize high-entropy alloy nanoparticles up to 15 elements at 2,073 K,[33] which has been considered a promising rapid synthesis technology for high-entropy materials with vast compositional space up to 3,000 K.[34,35] However, ultrafast synthesis of HECs at such high temperatures has seldom been reported.

To develop superior oxidation resistance of HECs by engineering their vast compositions, we design a new UHTS apparatus based on strong Joule heating that can reach a heating temperature of up to 3,273 K in seconds. By using this apparatus, the single-phase equiatomic 4- to 9-cation HECs of the IVB, VB, and VIB groups are successfully synthesized. Subsequently, the oxidation resistance of the as-synthesized HEC samples is investigated by thermal gravimetric analyzer-differential scanning calorimeter (TGA-DSC) analysis. Among the HEC samples, 6-cation HECs are proved to possess the best oxidation resistance. Further studies reveal that the superior oxidation resistance is mainly attributed to the formation of (Cr, Me)(Ta, Me)O_4 and (Cr, Me)$_2O_3$ (Me = Hf, Zr, Ta, Nb, Ti, and Cr) protective layers with low oxygen diffusion rates. This can effectively hinder the inward diffusion of oxygen as demonstrated by first-principles calculations.

RESULTS AND DISCUSSION

Characterization of as-synthesized HECs

For our self-developed UHTS apparatus, the synthesis temperature of the samples is greatly dependent on the heating power of the apparatus, which can be tuned by the cross-section area (*S*) of the graphite heater. As can be seen in Figure 1A, the increase in the synthesis temperature of HEC samples is proportional to the decrease in the *S* value. Particularly, a heating temperature of up to approximately 3,273 K can be achieved when *S* is down to 11 mm^2 (6.3 kW). Taking *S* = 19 mm^2 (a heating power of 3.6 kW) as an example (see Figure 1B), the temperature curves tested by the infrared thermometer and thermocouple match well with the one simulated by finite-element analysis (FEA), indicating the reliability of the temperature measurement in our self-developed UHTS apparatus. In addition, the temperature distribution in the heater is relatively homogeneous from the FEA results in Figure 1C, which is beneficial to synthesizing single-phase HECs with uniform compositions. All the HEC samples of the IVB, VB, and VIB groups were synthesized by the UHTS apparatus, namely ($Ta_{1/4}Nb_{1/4}Zr_{1/4}Ti_{1/4}$)C (4HEC), ($Ta_{1/5}Nb_{1/5}Zr_{1/5}Ti_{1/5}Hf_{1/5}$)C (5HEC), ($Ta_{1/6}Nb_{1/6}Zr_{1/6}Ti_{1/6}Hf_{1/6}Cr_{1/6}$)C (6HEC), ($Ta_{1/7}Nb_{1/7}Zr_{1/7}Ti_{1/7}Hf_{1/7}Cr_{1/7}Mo_{1/7}$)C (7HEC), ($Ta_{1/8}Nb_{1/8}Zr_{1/8}Ti_{1/8}Hf_{1/8}Cr_{1/8}Mo_{1/8}V_{1/8}$)C (8HEC), and ($Ta_{1/9}Nb_{1/9}Zr_{1/9}Ti_{1/9}Hf_{1/9}Cr_{1/9}Mo_{1/9}V_{1/9}W_{1/9}$)C (9HEC). According to our previous work,[28] the 4HECs can be produced by carbothermal reduction at 2,473 K, but this temperature is too low to synthesize HECs with more components, i.e., 5–9HECs. Therefore, 2,523 K is chosen as the initial synthesis temperature for synthesizing the remaining

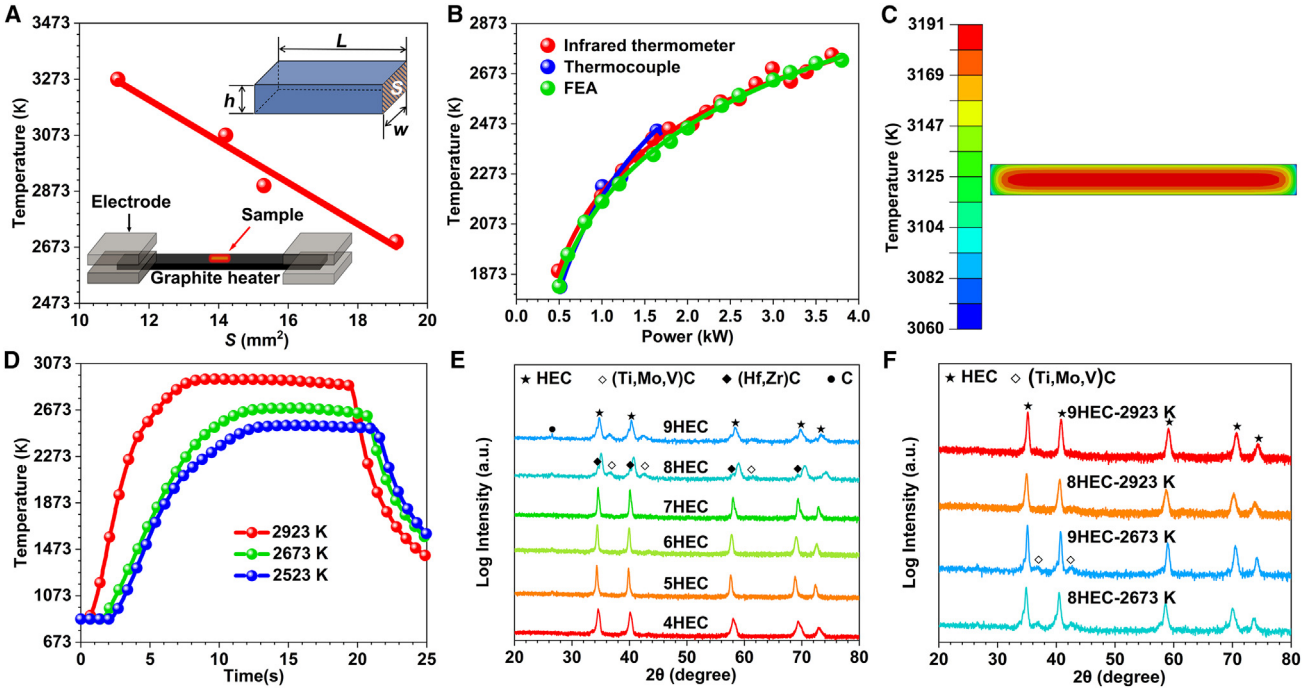

Figure 1. Design of UHTS apparatus and XRD analysis of as-synthesized 4–9HEC samples

(A) Temperature vs. *S* profiles of the graphite heater with alternating current (AC) = 240 A, where *w*, *h*, and *L* are the width, height, and length of the graphite heater, respectively.

(B) Temperature vs. power profiles of the graphite heater with an *S* of 19 mm^2 obtained by thermocouple, infrared thermometer, and FEA.

(C) The temperature distribution of a graphite heater simulated by FEA at a power of 6.3 kW.

(D) Heating temperature measured by an infrared thermometer vs. time profiles of the as-synthesized 4–9HEC samples at different conditions.

(E) XRD patterns of the as-synthesized 4–9HEC samples at 2,523 K.

(F) XRD patterns of the as-synthesized 8HEC and 9HEC samples at 2,673 and 2,923 K, respectively.

5–9HECs. Figure 1D shows the heating temperature vs. time profiles of the as-synthesized HEC samples at different conditions, measured by an infrared thermometer. A temperature of up to 2,923 K can be reached in seconds, demonstrating an ultrafast heating rate via our self-developed UHTS apparatus. X-ray diffraction (XRD) analysis was utilized to investigate the phase compositions of the obtained samples. As shown in Figure 1E, the single-phase 4–7HEC samples have been successfully synthesized at 2,523 K without any segregations, while minor (Ti, Mo, V)C and (Hf, Zr)C impurities have been detected in the 8HEC and 9HEC samples at this synthesis temperature, implying the synthesis difficulty of HECs with more elements. This phenomenon is in accordance with our previous studies, which demonstrate that the incorporation of atoms with significantly different atomic radii results in increased distortions and volume differences.[31] This, in turn, facilitates the element and/or phase segregation. To address this issue, a higher synthesis temperature is required to enhance the elemental diffusion coefficients, thereby promoting the formation of a single-phase solid solution with a uniform distribution of elements. In the present case, for instance, the volume difference for the 4HECs is 8.96%, while that value reaches 12.96% for the 9HECs. Consequently, a higher temperature of 2,923 K was applied to synthesize the single-phase 8HEC and 9HEC samples (see Figure 1F). These results demonstrate the effectiveness and feasibility of our self-developed UHTS apparatus. The structures of the as-obtained HEC samples are further ascertained by Rietveld refinement of XRD patterns, as shown in Figure S1. The small fitting parameters suggest that the 4–9HECs (refer to Figures S1A–S1F, respectively) are well-crystalline rock-salt structures with

evaluated lattice parameters (*a*) close to the average values of corresponding individual carbides (see Table S1), which verifies the successful synthesis of the 4–9HEC samples via our self-developed UHTS apparatus.

The morphology, particle size, and element distributions of the as-synthesized 4–9HEC samples were further investigated. Here, the as-synthesized 5HEC samples were chosen as an illustrative example. The scanning electron microscopy (SEM) image in Figure S2A shows that the as-synthesized 5HEC samples are composed of numerous irregular microsized particles. The laser particle size analyzer reveals that all the as-synthesized 4–9HEC samples possess comparable particle sizes of approximately 15 μm (Figure S2B). Moreover, the measured $D_v(50)$ and $D_v(90)$ values, which mean that the particle sizes are below 50% and 90% of the sample volumes, respectively, confirm the similar particle size distributions of the HEC samples. To analyze the metal element distributions of the as-synthesized 4–9HECs, energy-dispersive spectroscopy (EDS) mapping analysis was carried out. Homogeneous distributions of the metal elements in the as-synthesized 4–9HEC samples (Figures S3A–S3F, respectively) are confirmed without any aggregations on the microscale. The transmission electron microscopy (TEM) characterization was performed to further analyze the crystal structure and compositional uniformity of the as-synthesized 4–9HEC samples. Taking 5HEC samples as an example, the high-resolution TEM (HRTEM) image with the corresponding fast Fourier transform (FFT) analysis (Figure 2A) present a representative periodic lattice structure with an interplanar spacing of 0.262 nm, corresponding to {111} planes of the as-synthesized 5HEC samples. This suggests that the HEC samples belong to a rock-salt crystal structure of metal carbides. Additionally, the lattice parameter calculated by TEM analysis (a = 4.545 Å) is consistent with that (a = 4.510 Å) obtained by Rietveld refinement, which further confirms the successful synthesis of single-phase HECs. Figures 2B–2G present the scanning transmission electron microscopy (STEM) images and the corresponding EDS compositional maps of the as-synthesized 4–9HEC samples. Clearly, neither metal element segregations nor aggregations can be observed, validating that all metal elements are homogeneously distributed in the 4–9HEC particles on the nanoscale. Table S2 lists the atomic percentages of metal elements of the as-synthesized 4–9HEC samples, which are in good consistency with their stoichiometric ratios. Based on these observations, a conclusion can be drawn that the single-phase 4–9HEC samples with uniform compositions have been successfully synthesized via the self-developed UHTS apparatus.

Oxidation resistance

In order to investigate the oxidation resistance of the as-synthesized 4–9HEC samples, non-isothermal oxidation tests were performed from room temperature to 1,673 K. According to the weight change vs. temperature curves of the as-synthesized 6–9HEC samples, as illustrated in Figure 3A, the 4–6HEC samples begin to show drastic weight gains in the vicinity of 873 K and then remain almost unchanged with the further increased oxidation temperature. For the 7–9HEC samples, weights soar near 873 K as well but immediately reduce as the temperature further rises. The weight drops of the 7–9HEC samples should be correlated to the evaporation of the volatile oxides, such as MoO_3. The temperatures with maximum weight gain (T_m) of all HEC samples are listed in Table 1. Clearly, the 6HEC samples show the highest T_m value of 1,302 K, and the T_m of the 8HEC samples is the lowest (1,014 K), indicating that the oxides of the 6HEC samples are the most stable at high temperatures, while those of the 8HEC samples are inferior. Based on the T_m values of all HEC samples, the oxidation resistance of HEC samples is determined in the following order: 6HEC > 5HEC > 4HEC > 9HEC > 7HEC > 8HEC. As a result, the Cr element is

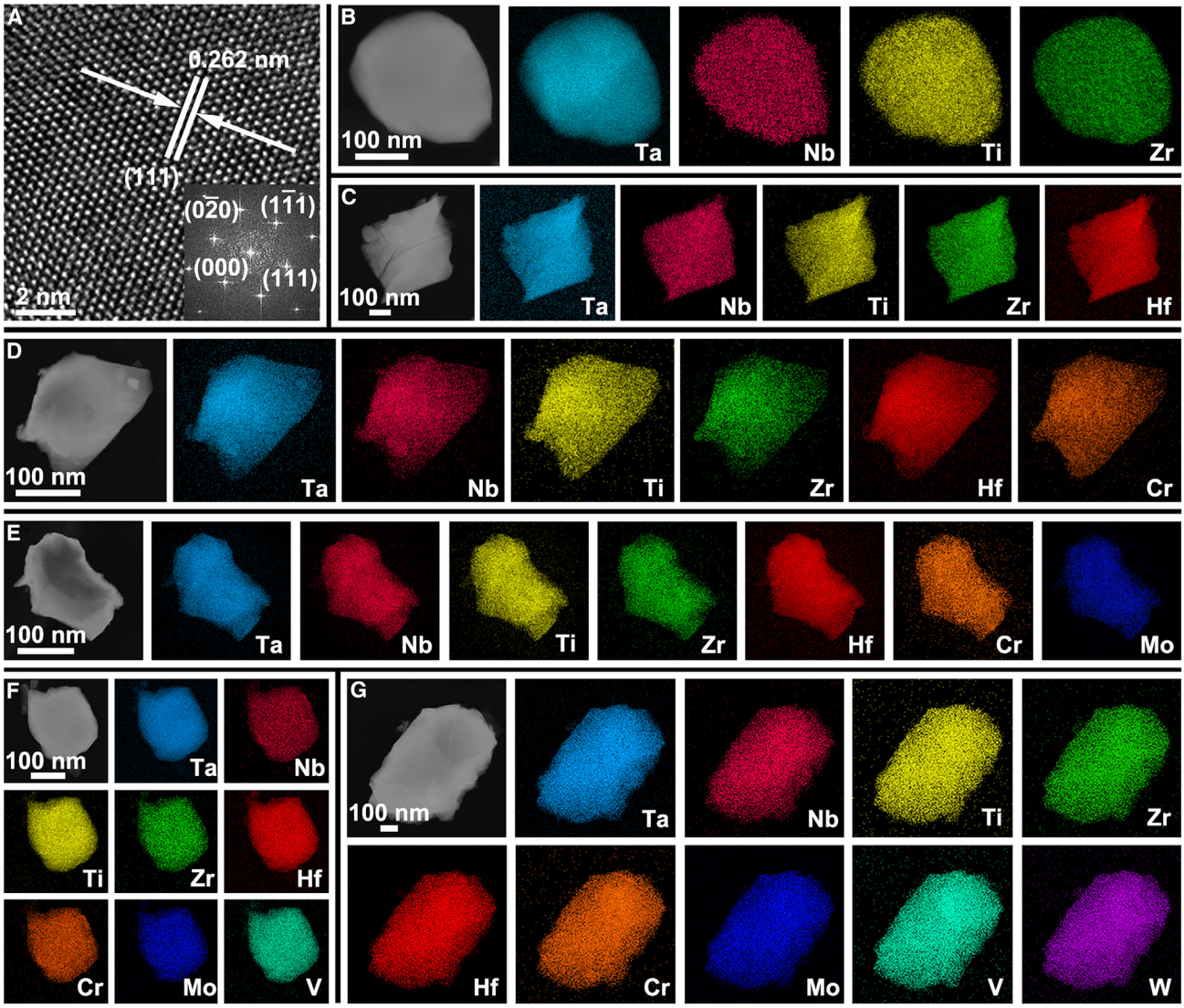

Figure 2. TEM analysis of as-synthesized 4–9HEC samples

(A) HRTEM image of the as-synthesized 5HEC samples. Inset is the corresponding FFT pattern. Scale bar, 2 nm.

(B–G) STEM images and corresponding EDS compositional maps of the as-synthesized 4–9HEC samples. Scale bars, 100 nm.

inferred to be beneficial to the oxidation resistance, followed by Hf and W elements, while Mo and V elements are both detrimental to the oxidation resistance. Figure 3B displays the DSC curves of the 4–9HEC samples as a function of oxidation temperature. It is notable that the appearance of DSC peaks indicates the exothermal reactions, which should be related to the severe oxidation of the HECs. The exothermic peak temperatures (T_e) of the 4–9HEC samples are listed in Table 1. It can be observed that the T_e shows a similar tendency to the T_m and that the 6HEC and 8HEC samples still possess the maximum and minimum values, respectively. Therefore, the order of oxidation resistance of the 4–9HEC samples has been confirmed.

Given the fact that the 4–6HEC samples all demonstrate relatively good oxidation resistance, they were further oxidized at 1,073 K for 120 min in air to investigate the oxidation resistance. As can be seen in Figures 3C and 3D, the 6HEC samples are fully oxidized after oxidation for 109 min, reaching a plateau stage. Meanwhile,

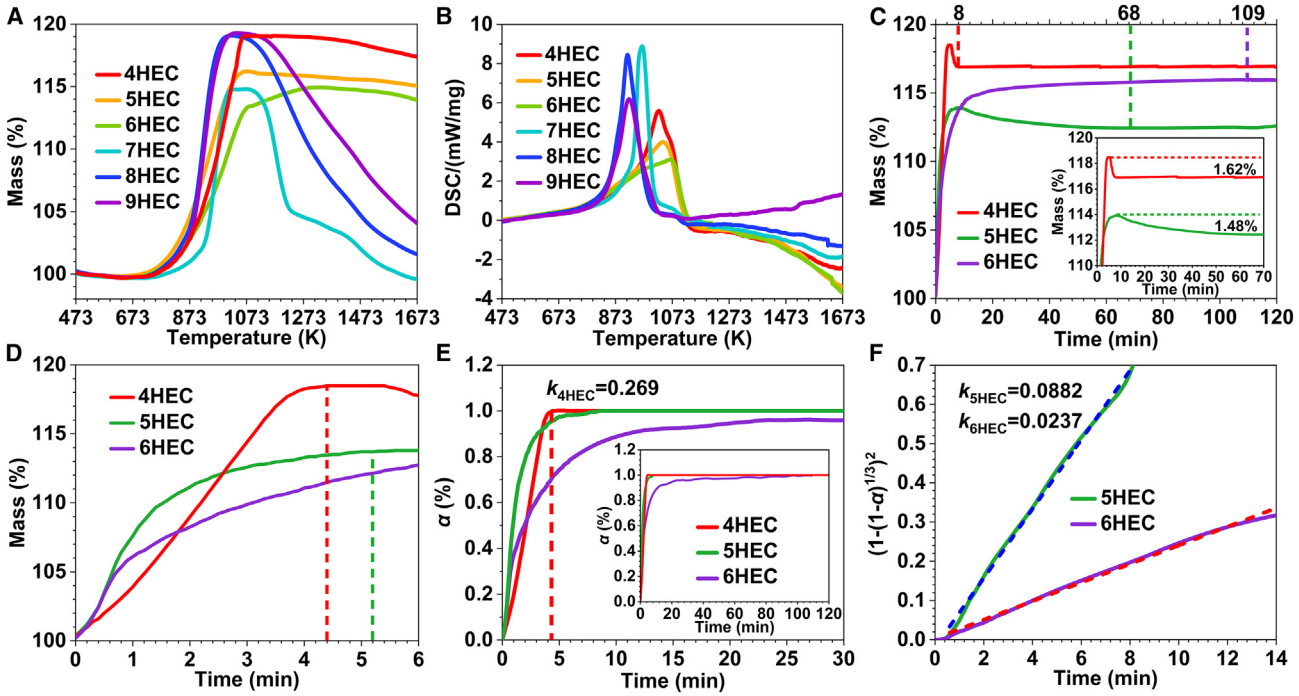

Figure 3. Oxidation tests of as-synthesized 4–9HEC samples

(A) Weight changes curves of the 4–9HEC samples as a function of oxidation temperatures.

(B) DSC curves of the 4–9HEC samples as a function of oxidation temperatures.

(C) Weight changes of the 4–6HEC samples as a function of oxidation time during isothermal oxidation at 1,073 K.

(D) Enlarged region of (C).

(E) α changes of the 4–6HEC samples as a function of time during isothermal oxidation at 1,073 K.

(F) Oxidation kinetics of the 5HEC and 6HEC samples based on Jander's equation.

the 4HEC and 5HEC samples suffer from severe oxidation and reach their maximum weight gains within the initial 6 min, followed by continuous weight losses with the prolonging of the oxidation process. Notably, the oxidation of the HECs is generally accompanied by phase segregation, namely the split of complicated oxides and carbon phases.[36] Hence, the weight drops of the HEC samples should be related to the oxidation of the carbon phase at the elevated temperature. In other words, the higher the diffusion inhabitation of the forming protective oxides to oxygen, the less oxidation the carbon phase suffers, and the less weight loss of HEC samples. The detailed oxidation curves of the 4HEC and 5HEC samples are shown in the inset of Figure 3C. Clearly, the 4HEC samples reach the final weight loss of 1.62% quickly, in the first 10 min. The dramatic weight loss of the 4HEC samples indicates that once the carbon phase is split and formed, it is immediately oxidized to release CO_2 due to the limited protective ability of the generated high-entropy oxides. By comparison, the 5HEC samples exhibit a much slower weight loss rate, reaching a weight loss value of 1.48% only after the oxidation has lasted for over 60 min. Thus, the generated carbon phase can be protected by the forming oxides and inhibited from the direct contact of oxygen to a great degree. Note that the 6HEC samples demonstrate continuous weight gain for 109 min without obvious signs of weight loss in the whole oxidation process, indicating that an oxide layer with superior protective ability should be formed to protect the underlying HECs. The results are also in good agreement with the TGA tests in Figure 3A. From the above analysis, it can be seen that metal elements play a key role in different weight changes of the HEC samples. Figure 3E shows the oxidation kinetics of the 4–6HEC samples. Obviously,

Table 1. Maximum mass oxidation temperature (T_m) and exothermic peak temperature (T_e) of the 4–9HEC samples during TGA tests

Samples	4HEC	5HEC	6HEC	7HEC	8HEC	9HEC
T_m (K)	1,066	1,076	1,302	1,020	1,014	1,035
T_e (K)	1,025	1,041	1,066	967	916	921

the 4HEC samples follow a linear relationship of oxidation degree (α) vs. oxidation time in the initial oxidation stage, while those of the 5HEC and 6HEC samples are near parabolic (more details about the calculation for the α are shown in the experimental procedures). The linear oxidation kinetic of the 4HEC samples indicates that almost no protective oxide layer is formed to hinder the diffusion of oxygen in the samples, leading to continuous oxidation at a constant rate. Regarding the 5HEC and 6HEC samples, protective oxide layers should be generated to prevent oxygen from diffusing inward, and thereby the oxidation is suppressed to some extent. The oxidation rate constants (k) of the 5HEC and 6HEC samples are calculated based on Jander's equation (refer to the experimental procedures). As depicted in Figure 3F, the 6HEC samples possess a slower k value of 0.0237 than that of the 5HEC samples (0.0882), which further confirms that the 6HEC samples possess the best oxidation resistance among all the HEC samples.

Oxidation mechanism

XRD analysis was applied to investigate the oxidation products of 4–6HEC samples after isothermal oxidation at 1,073 K. As shown in Figure 4A, the major oxidation product of the 4–6HEC samples is (Zr, Me)$_6$(Nb, Me)$_2$O$_{17}$ phase, and the minor impurity phase is (Ta, Me)$_2$O$_5$. In addition, the 4HEC and 5HEC samples contain a tiny amount of (Ti, Me)(Nb, Me)$_2$O$_7$ and (Ti, Me)(Ta, Me)O$_4$ phases, respectively, while the 6HEC samples have a small number of (Cr, Me)(Ta, Me)O$_4$ and (Cr, Me)$_2$O$_3$ phases. Combined with the oxidation kinetic in Figure 3E, it is speculated that the (Zr, Me)$_6$(Nb, Me)$_2$O$_{17}$ and (Ti, Me)(Nb, Me)$_2$O$_7$ phases have negative effect on the oxidation resistance of HECs considering the worst oxidation resistance of the 4HECs, while the (Ti, Me)(Ta, Me)O$_4$, (Cr, Me)(Ta, Me)O$_4$, and (Cr, Me)$_2$O$_3$ phases are beneficial to the oxidation resistance. It is worth mentioning that the contribution of (Cr, Me)(Ta, Me)O$_4$ and (Cr, Me)$_2$O$_3$ phases to the oxidation resistance is significantly greater than that of (Ti, Me)(Ta, Me)O$_4$ phase, indicating that the Cr element is advantageous to the oxidation resistance of the HECs. SEM-EDS analysis of the 6HEC samples after isothermal oxidation at 1,073 K was performed to further confirm the oxidation products (see Figures 4B and 4C). The metal elements are roughly uniform in the 6HEC samples. However, there are also some segregated regions, i.e., Cr- and Ta-rich regions. The corresponding EDS spot analysis results are listed in Table 2. Combined with the XRD results (Figure 4A), it is suggested that the spots 1, 2, and 3 in the 6HEC samples mainly consist of (Cr, Me)(Ta, Me)O$_4$, (Cr, Me)$_2$O$_3$, and (Zr, Me)$_6$(Nb, Me)$_2$O$_{17}$, respectively. In addition, (Ta, Me)$_2$O$_5$ phase can also be confirmed, as shown in Figures S4A and S4B. These results are in good agreement with those of XRD analysis, which further confirms the reliability of the XRD results.

To further investigate the inhibition effects of (Ti, Me)(Ta, Me)O$_4$, (Cr, Me)(Ta, Me)O$_4$, and (Cr, Me)$_2$O$_3$ layers on the oxygen diffusion, *ab initio* molecular dynamics (AIMD) analysis was carried out to obtain the mean square displacement (*MSD*) of oxygen atoms in (Ti, Me)(Ta, Me)O$_4$, (Cr, Me)(Ta, Me)O$_4$, and (Cr, Me)$_2$O$_3$ at 1,073 K. (Ti, Me)(Ta, Me)O$_4$, (Cr, Me)(Ta, Me)O$_4$, and (Cr, Me)$_2$O$_3$ were simplified as TiTaO$_4$, CrTaO$_4$, and Cr$_2$O$_3$, respectively, as the targets in our simulations due to the uncertainty and the limited effect of Me element rations. As displayed in Figure 4D, the

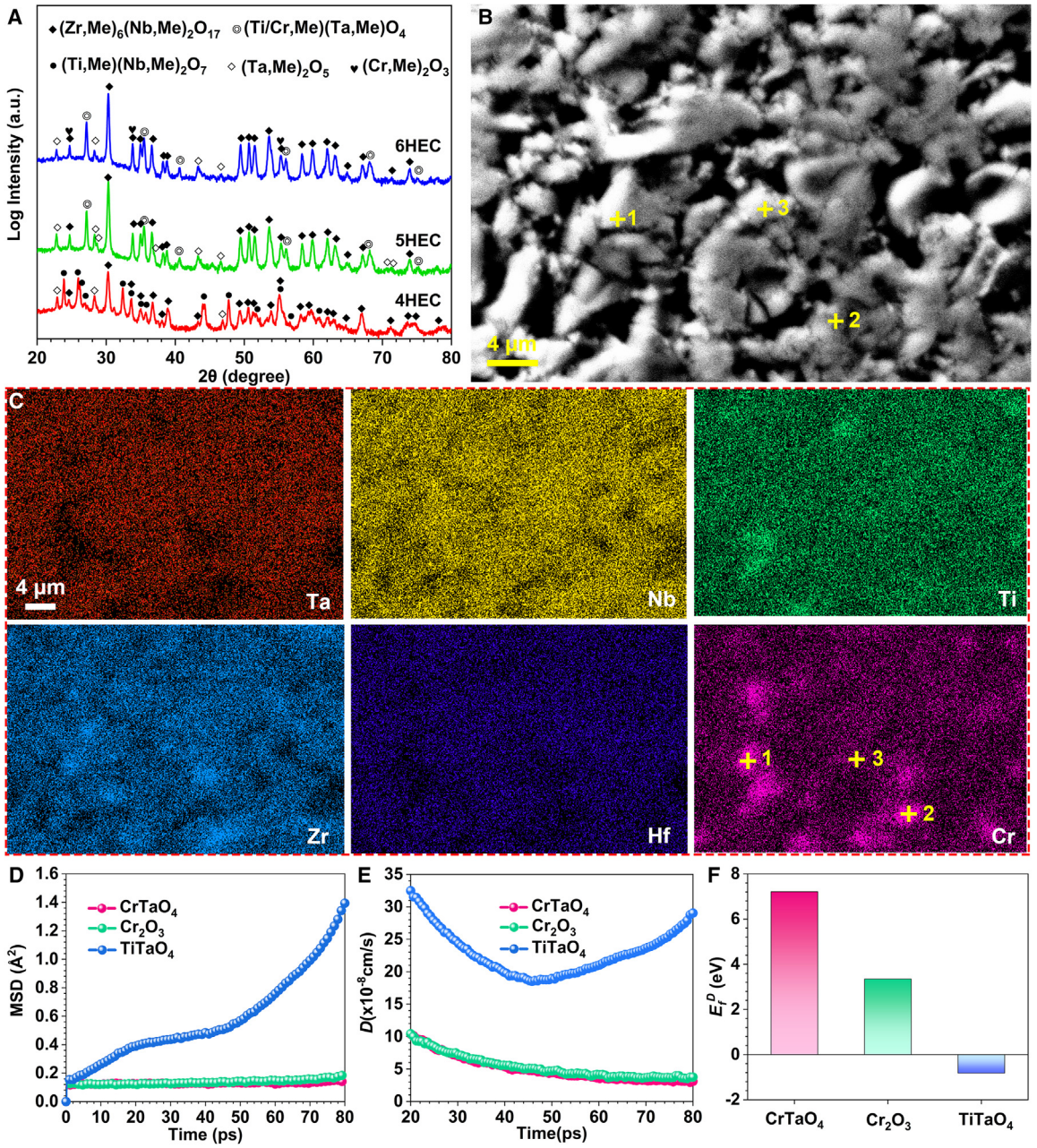

Figure 4. XRD and SEM analysis of the 4–6HEC samples after isothermal oxidation and first-principles calculations of oxygen diffusion in $CrTaO_4$, Cr_2O_3, and $TiTaO_4$ at 1,073 K

(A) XRD patterns of the 4–6HEC samples.

(B and C) SEM images (B) and corresponding EDS analysis (C) of the 6HEC samples. Scale bars, 4 μm.

(D and E) *MSD* (D) and *D* (E) of oxygen atoms in $CrTaO_4$, Cr_2O_3, and $TiTaO_4$.

(F) E_f^D of the oxygen in $CrTaO_4$, Cr_2O_3, and $TiTaO_4$.

interstitial oxygen atoms in $CrTaO_4$ and Cr_2O_3 show much lower *MSD* values than those in $TiTaO_4$. Furthermore, the oxygen diffusion coefficients (*D*) deduced from the *MSD* curves are exhibited in Figure 4E. Obviously, Cr_2O_3 and $CrTaO_4$ exhibit considerably lower *D* values compared to $TiTaO_4$, with average values of 5.70×10^{-8}, 4.96×10^{-8}, and 24.20×10^{-8} cm^2/s, respectively. All these results indicate a significantly improved barrier effect on oxygen diffusion for the $CrTaO_4$ and

Table 2. Element atomic percentages of different areas in 6HEC samples after oxidation at 1,073 K characterized by SEM-EDS analysis

	Elements (at %)							
Spots	Ta	Nb	Zr	Ti	Hf	Cr	O	Phase composition
1	4.51	3.80	4.45	4.28	0.83	8.65	72.89	(Cr, Me)(Ta, Me)O_4
2	2.31	2.91	3.13	3.28	1.77	25.13	61.45	(Cr, Me)$_2O_3$
3	4.18	6.43	4.84	4.46	4.45	4.05	71.59	(Zr, Me)$_6$(Nb, Me)$_2O_{17}$

Cr_2O_3. Thus, the incorporation of the Cr element causes a large enhancement in oxidation resistance, which is also consistent with the oxidation kinetics in Figure 3C. Furthermore, Figure 4F depicts the defective formation energies (E_f^D) of the oxygen in $CrTaO_4$, Cr_2O_3, and $TiTaO_4$ at 1,073 K. It is worth noting that both $CrTaO_4$ and Cr_2O_3 have positive E_f^D, while the value in $TiTaO_4$ is negative, indicating that the oxygen is more difficult to diffuse to form O interstitials in $CrTaO_4$ and Cr_2O_3. Hence, AIMD simulations also confirmed that the Cr element is advantageous to the oxidation resistance of HECs.

To further evaluate the microstructure evolutions of the 6HEC samples during oxidation, TEM characterization was carried out. In the initial oxidation stage, an amorphous phase (region I) was generated on the surface of 6HEC particles, as exhibited in Figures 5A and 5B. The corresponding amorphous structure can be identified by the selected-area electron diffraction pattern of region II (Figure 5C), which shows typical diffraction rings. Additionally, according to the EDS analysis of spot 1 (the corresponding element atomic percentages are listed in Table S3), the amorphous phase mainly consists of C and O elements. These results confirm the generation of amorphous carbon structure in the 6HEC samples during oxidation. In addition, Figure 5D depicts the HRTEM image of region III in Figure 5A, from which a layer-ordered structure with a local interlayer spacing of 0.350 nm can be seen on the oxidized particle surface. This structure demonstrates the generated ordered graphite with {002} planes. In the middle oxidation stage, as exhibited in Figure 5E, there are multiple lattice stripes, representing the generation of various oxidation products. The enlarged regions IV–VI with corresponding FFT analysis (Figures 5F–5H, respectively) show that the typical periodic lattice structures have fringes with the interplanar spacings of 0.164, 0.357, and 0.246 nm, corresponding to the {220}, {111}, and {200} planes of $CrTaO_4$, Cr_2O_3, and $Zr_6Nb_2O_{17}$, respectively. The calculated lattice parameters (*a*, *b*, and *c*) of $CrTaO_4$, Cr_2O_3, and $Zr_6Nb_2O_{17}$ are close to the complicated oxide solid solutions of 6HEC samples (*a*′, *b*′, and *c*′, as listed in Table 3). These results further confirm that oxidation products of 6HEC samples mainly consist of (Cr, Me)$_2O_3$, (Cr, Me)(Ta, Me)O_4, and (Zr, Me)$_6$(Nb, Me)$_2O_{17}$ phases. In the final oxidation stage, as illustrated in Figures 5I and 5J, the elemental segregations and aggregations occur, and 6HEC particles have been divided into two regions, namely Cr- and Nb-rich regions. Combined with the EDS analysis results listed in Table 3, it can be inferred that the Nb-rich region is (Zr, Me)$_6$(Nb, Me)$_2O_{17}$ phase and that the Cr-rich region mainly consists of (Cr, Me)$_2O_3$ and (Cr, Me)(Ta, Me)O_4 phases.

Based on the above results, the potential oxidation resistance mechanism of the 6HEC samples is schematically shown in Figure 6. Compared to the original particles (Figure 6A), in the initial oxidation stage (Figure 6B), carbon phases including amorphous carbons and ordered graphites become apparent on the surface of the 6HEC particles due to the diffusion and rearrangement of carbon atoms at the elevated temperatures.[17] At this condition, oxygen will react with the exposed carbon layers to release CO_2. After the complete consumption of carbons, the oxygen diffuses in

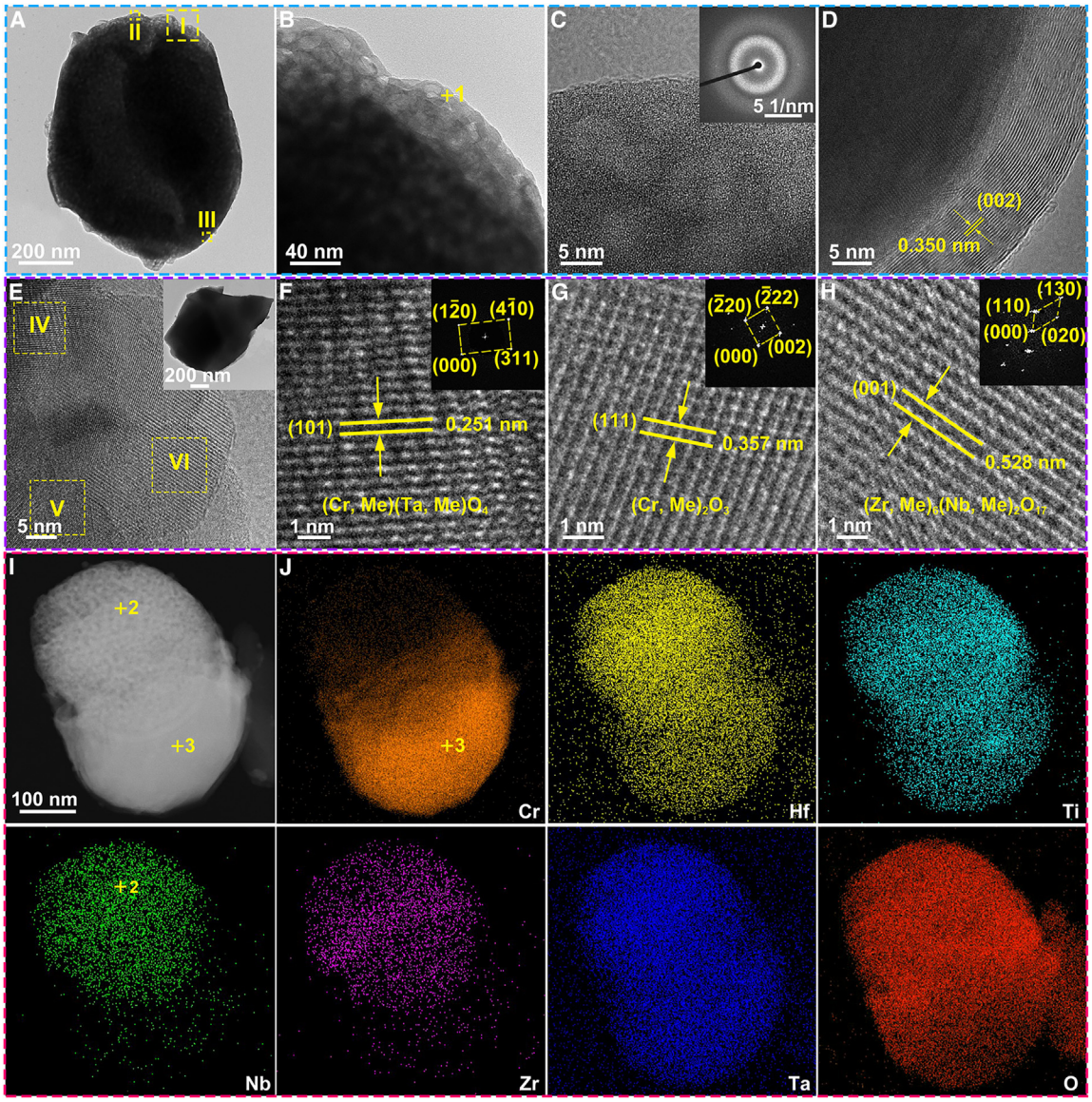

Figure 5. TEM analysis of 6HEC samples after isothermal oxidation at 1,073 K

(A–D) TEM image of 6HEC particles in the initial oxidation stage (A) and HRTEM images of (A) in regions I (B), II (C), and III (D). Scale bars, 200 nm (A), 40 nm (B), and 5 nm (C and D).

(E–H) HRTEM image of 6HEC particles in the middle oxidation stage (E) and HRTEM images of oxidation products in regions IV (F), V (G), and VI (H) inset with the corresponding FFT patterns. Scale bars, 5 nm (E) and 1 nm (F–H).

(I and J) STEM image (I) and corresponding EDS compositional maps (J) of 6HEC particles in the final oxidation stage. Scale bar, 100 nm.

and reacts with the underlying ceramic to form the high-entropy oxycarbide (HECO) layer.[36] With the continuous diffusion of oxygen into the HECO, the layer is then oxidized into complex transition-metal oxides involving (Cr, Me)$_2$O$_3$, (Cr, Me)(Ta, Me)O$_4$, and (Zr, Me)$_6$(Nb, Me)$_2$O$_{17}$ phases. These complicated oxides are preliminarily established as a protective layer to hinder the inward diffusion of oxygen in the middle oxidation stage (Figure 6C). As the oxidation proceeds, due to the smaller cationic radius of Cr^{3+}, the Cr elements can segregate and diffuse outward to form the Cr-rich protective oxides (namely the (Cr, Me)$_2$O$_3$ and (Cr, Me)(Ta, Me)O$_4$ phases) on the surface of samples. The formed outside protective layer with a great amount of (Cr, Me)$_2$O$_3$ and (Cr, Me)(Ta, Me)O$_4$ phases can effectively inhibit the

Table 3. Lattice parameters of complicated oxides (*a*, *b*, and *c*) and corresponding solid solutions of 6HEC samples (*a′*, *b′*, and *c′*) calculated based on the TEM analysis

Phases	Space groups	*a*	*a′*	*b*	*b′*	*c*	*c′*
(Cr, Me)(Ta, Me)O_4	$P4_2/mnm$	4.645	4.639	4.645	4.639	3.019	–
(Cr, Me)$_2O_3$	$R\bar{3}c$	5.358	5.332	5.358	5.332	5.358	5.332
(Zr, Me)$_6$(Nb, Me)$_2O_{17}$	*Ima2*	4.964	4.928	5.120	–	5.289	5.435

inward oxygen diffusion due to their low oxygen diffusion coefficients and good barrier effects (Figure 6D). Although the Cr-rich protective oxide layer can slow down the oxidation rate of the 6HEC samples to a great extent, oxygen can still diffuse through the micropores left by the escape of generated CO_2 to react with the residual 6HECs. As a result, the 6HEC samples are completely transformed into oxide particles finally (Figure 6E). According to the TEM analysis in Figure 5, the final oxidation products of 6HECs are not uniform: the innermost of the 6HEC samples should be composed of the (Zr, Me)$_6$(Nb, Me)$_2O_{17}$ primary phase as well as a small number of (Cr, Me)$_2O_3$ and (Cr, Me)(Ta, Me)O_4 phases, while the outermost is mainly made of (Cr, Me)$_2O_3$ and (Cr, Me)(Ta, Me)O_4 phases.

EXPERIMENTAL PROCEDURES

Resource availability

Lead contact

Further information requests should be directed to and will be fulfilled by the lead contact, Yanhui Chu (chuyh@scut.edu.cn).

Materials availability

This study did not generate new unique materials.

Data and code availability

All of the data supporting this study are available in this article and its supplemental information.

Design of UHTS apparatus

A UHTS apparatus was designed based on intense Joule heating to achieve the heating temperature of 3,273 K within seconds, which included the molybdenum electrodes and a graphite heater (IG-56, Toyo Tanso, Shanghai, China), as displayed in the inset of Figure 1A. Different heating temperatures can be realized by adjusting the *S* of the graphite heater, as well as the output current and voltage, which were measured by the infrared thermometer (GmbH M313, SensorTherm, Steinbach, Germany) and the W-Re thermocouple. In order to further analyze the heating effects of the graphite heater, the heating-temperature distribution of the graphite heater was simulated by FEA. A transient heat production model (1.6 × 6.8 × 130.0 mm) containing 3,696 elements was established by ABAQUS.[37] The heating power was computed based on the output current and voltage, and the 3-dimensional body heating source was adopted to simulate the generation of Joule heating. The heat conduction analysis was calculated by the following heat balance equation[37]:

$$\frac{\partial T}{\partial t} = \frac{\lambda}{\rho C_P}\left(\frac{\partial^2 T}{\partial x^2} + \frac{\partial^2 T}{\partial y^2} + \frac{\partial^2 T}{\partial z^2}\right) + \frac{\dot{q}}{\rho C_P}, \qquad \text{(Equation 1)}$$

where C_P, ρ, T, λ, and t are the specific heat, density, element temperature, thermal conductivity, and time, respectively, and $\dot{q}$ is heat flux. x, y, and z are the geometric coordinates of the finite-element model. With respect to the thermal boundary conditions, thermal radiation scattering and thermal convection heat dissipation were

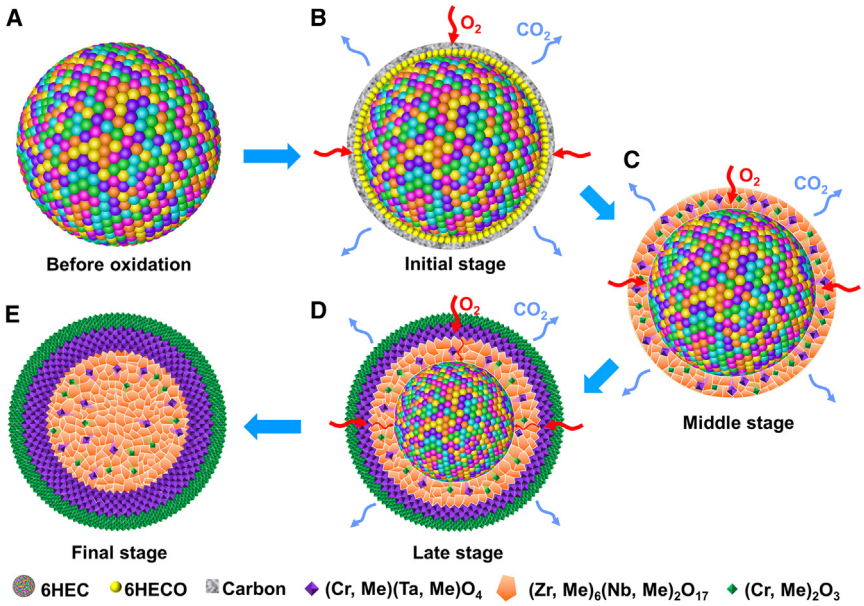

Figure 6. Schematic of potential oxidation resistance mechanism of 6HEC samples

(A) Before oxidation.

(B) Initial stage.

(C) Middle stage.

(D) Late stage.

(E) Final stage.

considered to simulate the real experimental conditions, which can be described by the equilibrium equations as follows[38]:

$$\frac{\partial T}{\partial x}n_x + \frac{\partial T}{\partial y}n_y + \frac{\partial T}{\partial z}n_z = h_c(T_\infty - T) + \varepsilon\sigma_0\left(T_\infty^4 - T^4\right) \quad \text{(Equation 2)}$$

where n_x, n_y, and n_z are the outer normal direction cosines of the boundary, h_c is the surface heat transfer coefficient, T_∞ is the ambient temperature, ε is the emissivity, and σ_0 is the Stefan-Boltzmann constant.

Synthesis of 4–9HEC samples

The equiatomic 4–9HECs were synthesized via carbothermic reduction. The commercially available metal oxides and carbon powders were used as the raw materials. Detailed information on the raw materials is listed in Tables S3 and S4. The transition-metal oxide powders and carbon powders were milled by hand for 30 min in an agate mortar based on the corresponding molar ratios of HECs. Afterward, the mixed powders were pressed into pellets of 6 (diameter) × 2 (thickness) mm under a uniaxial pressure of 10 MPa before being wrapped in graphite paper. The as-pressed pellets were then placed on the graphite heater. Subsequently, alternating current (100-250A) was applied to both ends of the graphite rod to heat these pellets to the desired temperatures within seconds under a vacuum below 5×10^{-3} Pa. After the sustained heating for a certain time, the power was turned off, the samples were rapidly cooled to room temperature, and then they were taken out and ground in an agate mortar to obtain the as-synthesized HEC samples.

Oxidation tests of as-synthesized 4-9HEC samples

The oxidation behaviors of the as-synthesized HEC samples were investigated by TGA (TGA/SDTA 851, Metter Toledo Star, Zurich, Switzerland) tests. With respect

to the non-isothermal oxidation tests, the as-synthesized HEC samples were heated from room temperature to the desired oxidation temperature at a heating rate of 10 K/min in the air. With respect to the isothermal oxidation tests, the as-synthesized HEC samples were firstly heated up to 1,073 K at a heating rate of 10 K/min under the argon atmosphere and then kept in the air for 120 min. TGA curves were used to record the mass changes of the samples related to the oxidation temperature, and DSC mode was applied to record the heat flow rate changes per mass. Herein, the oxidation degree α was used to evaluate the isothermal oxidation behaviors of the as-synthesized HEC samples, and oxidation kinetics was analyzed based on Jander's equation[36]:

$$\alpha = \frac{w_i - w_0}{w_f - w_0} \times 100\% \quad \text{(Equation 3)}$$

$$\left[1 - (1 - \alpha)^{1/3}\right]^2 = kt, \quad \text{(Equation 4)}$$

where w_0, w_i, and w_f correspond to the initial, intermediate, and final mass, respectively. k is the oxidation rate constant, and t is the oxidation time.

Characterization

The particle size distribution of the samples was characterized by a laser particle size analyzer (Zhuhai OMEC Instruments, Zhuhai, China). The phase compositions, microstructure, and element distribution of the samples were characterized by XRD (X'pert PRO; PANalytical, Almelo, the Netherlands), SEM (Supra-55; Zeiss, Oberkochen, Germany) equipped with EDS, and TEM (Themis Z; FEI, Eindhoven, the Netherlands) equipped with EDS. The Rietveld refinement was carried out via the general structure analysis system software.

Theoretical calculations

To explore the mechanism of oxidation resistance, density functional theory calculations were implemented in the Vienna Ab initio Simulation Package.[39] The projector-augmented wave pseudopotentials[40] were applied to describe the interactions between electrons and ions with the generalized gradient approximation by Perdew-Burke-Ernzerhof functional.[41] The special quasi-random structure (SQS) approach was adopted in the Alloy Theoretic Automated Toolkit to mimic the complete chemically disordered crystal structures.[42] Based on the space group of $P4_2/mnm$, 1 × 2 × 3 SQS supercells were generated for both $CrTaO_4$ and $TiTaO_4$. In all calculations, the spin-polarization effects were taken into consideration with a plane-wave energy cutoff of 520 eV. The convergence criterion of electronic steps was set to 10^{-4} eV, and the Brillouin zones were sampled by a density of 0.3 $Å^{-1}$ with the Γ-centered method.[43] For AIMD simulations, 2 × 2 × 2 supercells were further generated from fully relaxed $CrTaO_4$/$TiTaO_4$ SQS supercells and Cr_2O_3, respectively. One oxygen atom was added to the models at the most favorable interstitial site to mimic 2% oxygen defects. Only Γ point was used in AIMD calculations, and a total period of 80 ps with a time step of 2 fs was applied under the NVT ensemble.[44] The initial 20 ps was used to equilibrate the system, and data for diffusivities were collected from the subsequent 60 ps. D of $CrTaO_4$, $TiTaO_4$, and Cr_2O_3 were calculated by the following equation[45]:

$$D = \frac{1}{2d} \lim_{t \to \infty} \frac{d}{dt} MSD \quad \text{(Equation 5)}$$

where d equals the dimension of the oxide lattice on which diffusion takes place and t is time. In addition, $E_f^D[X]$ of $CrTaO_4$, $TiTaO_4$, and Cr_2O_3 were computed by the following equation[46]:

$$E_f^D[X] = E_{tot}^D[X] - E_{tot}^0[X] - E[O] \quad \text{(Equation 6)}$$

where $E_{tot}^D[X]$ and $E_{tot}^0[X]$ are the total amounts of energy derived from defected and perfect $CrTaO_4/TiTaO_4$ and Cr_2O_3, respectively. $E[O]$ refers to the energy of an oxygen atom in the oxygen molecule.

SUPPLEMENTAL INFORMATION

Supplemental information can be found online at https://doi.org/10.1016/j.xcrp.2024.101821.

ACKNOWLEDGMENTS

We acknowledge financial support from the National Key Research and Development Program of China (no. 2021YFA0715801), the National Natural Science Foundation of China (no. 52122204 and 51972116), and the Guangzhou Basic and Applied Basic Research Foundation (no. 202201010632).

AUTHOR CONTRIBUTIONS

Y.C. conceived and designed this work. Z.W., Z.T., and L.Z. performed the experiments. H.M. performed the first-principles calculations. Y.C., L.Z., and Z.W. analyzed the data and wrote the manuscript. All authors commented on the manuscript.

DECLARATION OF INTERESTS

The authors declare no competing interests.

Received: December 4, 2023
Revised: January 6, 2024
Accepted: January 17, 2024
Published: February 14, 2024

REFERENCES

1. Rost, C.M., Sachet, E., Borman, T., Moballegh, A., Dickey, E.C., Hou, D., Jones, J.L., Curtarolo, S., and Maria, J.P. (2015). Entropy-stabilized oxides. Nat. Commun. *6*, 8485.
2. Ye, B., Wen, T., Nguyen, M.C., Hao, L., Wang, C.Z., and Chu, Y. (2019). First-principles study, fabrication and characterization of $(Zr_{0.25}Nb_{0.25}Ti_{0.25}V_{0.25})C$ high-entropy ceramics. Acta Mater. *170*, 15–23.
3. Oses, C., Toher, C., and Curtarolo, S. (2020). High-entropy ceramics. Nat. Rev. Mater. *5*, 295–309.
4. Sarkar, A., Velasco, L., Wang, D., Wang, Q., Talasila, G., de Biasi, L., Kübel, C., Brezesinski, T., Bhattacharya, S.S., Hahn, H., and Breitung, B. (2018). High-entropy oxides for reversible energy storage. Nat. Commun. *9*, 3400.
5. Ma, M., Han, Y., Zhao, Z., Feng, J., and Chu, Y. (2023). Ultrafine-grained high-entropy zirconates with superior mechanical and thermal properties. J. Materiomics. *9*, 370–377.
6. Gild, J., Zhang, Y., Harrington, T., Jiang, S., Hu, T., Quinn, M.C., Mellor, W.M., Zhou, N., Vecchio, K., and Luo, J. (2016). High-entropy metal diborides: A new class of high-entropy materials and a new type of ultrahigh temperature ceramics. Sci. Rep. *6*, 37946.
7. Liu, D., Wen, T., Ye, B., and Chu, Y. (2019). Synthesis of superfine high-entropy metal diboride powders. Scripta Mater. *167*, 110–114.
8. Ma, M., Ye, B., Han, Y., Sun, L., He, J., and Chu, Y. (2020). High-pressure sintering of ultrafine-grained high-entropy diboride ceramics. J. Am. Ceram. Soc. *103*, 6655–6658.
9. Gaboardi, M., Monteverde, F., Saraga, F., Aquilanti, G., Feng, L., Fahrenholtz, W., and Hilmas, G. (2022). Local structure in high-entropy transition metal diborides. Acta Mater. *239*, 118294.
10. Ma, M., Yang, X., Meng, H., Zhao, Z., He, J., and Chu, Y. (2023). Nanocrystalline high-entropy hexaboride ceramics enable remarkable performance as thermionic emission cathodes. Fundam. Res. *3*, 979–987.
11. Ye, B., Wen, T., Huang, K., Wang, C.Z., and Chu, Y. (2019). First-principles study, fabrication, and characterization of $(Hf_{0.2}Zr_{0.2}Ta_{0.2}Nb_{0.2}Ti_{0.2})C$ high-entropy ceramic. J. Am. Ceram. Soc. *102*, 4344–4352.
12. Wang, F., Yan, X., Wang, T., Wu, Y., Shao, L., Nastasi, M., Lu, Y., and Cui, B. (2020). Irradiation damage in $(Zr_{0.25}Ta_{0.25}Nb_{0.25}Ti_{0.25})C$ high-entropy carbide ceramics. Acta Mater. *195*, 739–749.
13. Wang, Y., Csanádi, T., Zhang, H., Dusza, J., Reece, M.J., and Zhang, R.Z. (2020). Enhanced hardness in high-entropy carbides through atomic randomness. Adv. Theory Simul. *3*, 2000111.
14. Ma, M., Hu, X., Meng, H., Zhao, Z., Chang, K., and Chu, Y. (2022). High-entropy metal carbide nanowires. Cell Rep. Phys. Sci. *3*, 100839.
15. Zhang, J., Xu, B., Xiong, Y., Ma, S., Wang, Z., Wu, Z., and Zhao, S. (2022). Design high-entropy carbide ceramics from machine learning. npj Comput. Mater. *8*, 5.
16. Chu, Y., Yu, R., He, G., Zhang, T., Dong, H., Deng, S., and Li, J. (2022). Combustion synthesis of high-entropy carbide nanoparticles for tetracycline degradation via persulfate activation. Sci. China Mater. *65*, 3144–3149.
17. Ma, M., Sun, Y., Wu, Y., Zhao, Z., Ye, L., and Chu, Y. (2022). Nanocrystalline high-entropy carbide ceramics with improved mechanical properties. J. Am. Ceram. Soc. *105*, 606–613.
18. He, L., Zhang, J., Li, Z., Lin, N., Liu, B., Zhao, S., Jin, K., Chen, H., Yan, H., Peng, F., et al. (2022). Toughening (NbTaZrW)C high-entropy carbide ceramic through Mo doping. J. Am. Ceram. Soc. *105*, 5395–5407.

19. He, L., Liu, L., Peng, F., Zhang, W., Lin, N., Zhao, S., Ma, Y., and Wu, Z. (2023). Host lattice and solid solution formation in an octal-cation (NbTaZrTiHfVWMo)C high entropy carbide ceramic. J. Eur. Ceram. Soc. *43*, 5792–5801.

20. Yan, X., Constantin, L., Lu, Y., Silvain, J.F., Nastasi, M., and Cui, B. (2018). $Hf_{0.2}Zr_{0.2}Ta_{0.2}Nb_{0.2}Ti_{0.2}$)C high-entropy ceramics with low thermal conductivity. J. Am. Ceram. Soc. *101*, 4486–4491.

21. Ye, B., Wen, T., Liu, D., and Chu, Y. (2019). Oxidation behavior of ($Hf_{0.2}Zr_{0.2}Ta_{0.2}Nb_{0.2}Ti_{0.2}$)C high-entropy ceramics at 1073-1473 K in air. Corrosion Sci. *153*, 327–332.

22. Ye, B., Wen, T., and Chu, Y. (2019). High-temperature oxidation behavior of ($Hf_{0.2}Zr_{0.2}Ta_{0.2}Nb_{0.2}Ti_{0.2}$)C high-entropy ceramics in air. J. Am. Ceram. Soc. *103*, 500–507.

23. Wang, Y., Zhang, R.Z., Zhang, B., Skurikhina, O., Balaz, P., Araullo-Peters, V., and Reece, M.J. (2020). The role of multi-elements and interlayer on the oxidation behaviour of (Hf-Ta-Zr-Nb)C high entropy ceramics. Corrosion Sci. *176*, 109019.

24. Wang, Y., and Reece, M.J. (2021). Oxidation resistance of (Hf-Ta-Zr-Nb)C high entropy carbide powders compared with the component monocarbides and binary carbide powders. Scripta Mater. *193*, 86–90.

25. Backman, L., Gild, J., Luo, J., and Opila, E.J. (2020). Part II: Experimental verification of computationally predicted preferential oxidation of refractory high entropy ultra-high temperature ceramics. Acta Mater. *197*, 81–90.

26. Tan, Y., Teng, Z., Jia, P., Zhou, X., and Zhang, H. (2021). Diverse oxidation behaviors of metal carbide solutions in high-temperature water vapor. Corrosion Sci. *191*, 109758.

27. Mellor, W.M., Kaufmann, K., Dippo, O.F., Figueroa, S.D., Schrader, G.D., and Vecchio, K.S. (2021). Development of ultrahigh-entropy ceramics with tailored oxidation behavior. J. Eur. Ceram. Soc. *41*, 5791–5800.

28. Ye, B., Ning, S., Liu, D., Wen, T., and Chu, Y. (2019). One-step synthesis of coral-like high-entropy metal carbide powders. J. Am. Ceram. Soc. *102*, 6372–6378.

29. Feng, L., Fahrenholtz, W.G., Hilmas, G.E., and Zhou, Y. (2019). Synthesis of single-phase high-entropy carbide powders. Scripta Mater. *162*, 90–93.

30. Ning, S., Wen, T., Ye, B., and Chu, Y. (2020). Low-temperature molten salt synthesis of high-entropy carbide nanopowders. J. Am. Ceram. Soc. *103*, 2244–2251.

31. Wen, T., Ye, B., Liu, H., Ning, S., Wang, C.Z., and Chu, Y. (2020). Formation criterion for binary metal diboride solid solutions established through combinatorial methods. J. Am. Ceram. Soc. *103*, 3338–3348.

32. Meng, H., Yu, R., Tang, Z., Wen, Z., and Chu, Y. (2023). Formation ability descriptors for high-entropy carbides established through high-throughput methods and machine learning. Cell Rep. Phys. Sci. *4*, 101512.

33. Yao, Y., Huang, Z., Xie, P., Lacey, S.D., Jacob, R.J., Xie, H., Chen, F., Nie, A., Pu, T., Rehwoldt, M., et al. (2018). Carbothermal shock synthesis of high-entropy-alloy nanoparticles. Science *359*, 1489–1494.

34. Wang, C., Ping, W., Bai, Q., Cui, H., Hensleigh, R., Wang, R., Brozena, A.H., Xu, Z., Dai, J., Pei, Y., et al. (2020). A general method to synthesize and sinter bulk ceramics in seconds. Science *368*, 521–526.

35. Xie, H., Qin, M., Hong, M., Rao, J., Guo, M., Luo, J., and Hu, L. (2022). Rapid liquid phase-assisted ultrahigh-temperature sintering of high-entropy ceramic composites. Sci. Adv. *8*, eabn8241.

36. Wen, Z., Tang, Z., Meng, H., and Chu, Y. (2022). A promising new class of high-entropy ceramics: High-entropy oxycarbides with good oxidation resistance. Corrosion Sci. *207*, 110574.

37. Yaakoubi, M., Kchaou, M., and Dammak, F. (2013). Simulation of heat treatment and materials with the use of the abaqus software. Met. Sci. Heat Treat. *55*, 386–392.

38. George, S. (2015). Heat Transfer Modeling: A Inductive Approach (New York: Springer).

39. Kresse, G., and Furthmüller, J. (1996). Efficiency of ab-initio total energy calculations for metals and semiconductors using a plane-wave basis set. Comput. Mater. Sci. *6*, 15–50.

40. Blöchl, P. (1994). Projector augmented-wave method. Phys. Rev. B *50*, 17953–17979.

41. Perdew, J.P., Burke, K., and Ernzerhof, M. (1996). Generalized gradient approximation made simple. Phys. Rev. Lett. *77*, 3865–3868.

42. Zunger, A., Wei, S., Ferreira, L.G., and Bernard, J.E. (1990). Special quasirandom structures. Phys. Rev. Lett. *65*, 353–356.

43. Monkhorst, H.J., and Pack, J.D. (1976). Special points for Brillouin-zone integrations. Phys. Rev. B *13*, 5188–5192.

44. van de Walle, A. (2009). Multicomponent multisublattice alloys, nonconfigurational entropy and other additions to the alloy theoretic automated toolkit. Calphad *33*, 266–278.

45. Mo, Y., Ong, S.P., and Ceder, G. (2012). First principles study of the $Li_{10}GeP_2S_{12}$ lithium super ionic conductor material. Chem. Mater. *24*, 15–17.

46. Yu, H., Shaikh, A.R., Xiong, F., and Chen, Y. (2018). Enhanced out-of-plane electrical transport in n-type SnSe thermoelectrics induced by resonant states and charge delocalization. ACS Appl. Mater. Interfaces *10*, 9889–9893.